Fast-beam measurements of the $10D$-$10F$ fine-structure intervals in helium

Nelson E. Claytor*
Department of Physics, University of Notre Dame, Notre Dame, Indiana 46556

E. A. Hessels
Department of Physics and Astronomy, York University, 4700 Keele Street, North York, Ontario, Canada M3J 1P3

S. R. Lundeen
Department of Physics, Colorado State University, Fort Collins, Colorado 80523
(Received 26 October 1994)

Four fine-structure intervals separating the $n=10$, $L=2$ and 3 Rydberg states of helium have been measured using a fast-beam microwave-optical technique. These are found to agree both with previous measurements of these intervals and with high-precision calculations. The experimental results for the four intervals are $10\,^1D_2-10\,^+F_3$, 10 918.826(37) MHz; $10\,^3D_1-10\,^3F_2$, 15 760.667(17) MHz; $10\,^3D_2-10\,^-F_3$, 15 770.704(15) MHz; and $10\,^3D_3-10\,^3F_4$, 15 781.991(11) MHz. The ^+F (^-F) state is the mixed singlet-triplet state of higher (lower) energy. The result for the spin-averaged $10D$-$10F$ interval in helium is 14 560.650(13) MHz, which has an experimental uncertainty of better than one part per million. The good agreement with theory breaks the pattern of discrepancies between theory and experiment observed in measurements of the higher-L $n=10$ helium fine structure. Possible explanations for those discrepancies are discussed.

PACS number(s): 32.30.Bv, 31.30.Jv

I. INTRODUCTION

The precision spectroscopy of Rydberg states of helium provides an exceptional opportunity to test the physics of two-electron atoms. Both the theory of and the experiments on these states have a long history, a review of which is found in Ref. [1]. The earliest experimental work on the "high-L" ($L>4$, where L is the orbital angular momentum of the Rydberg electron) Rydberg states of helium (in fact, of any atom) was reported in 1978 by Beyer and Kollath [2]. Experimental studies of low-L Rydberg states of helium were performed by Lamb and co-workers [3–5], using a microwave-optical resonance technique in which the Zeeman shifts of the resonances in an applied magnetic field were varied while the microwave frequency was kept fixed. These measurements were developed into an extensive series of precision microwave-optical measurements by MacAdam and coworkers [6–9], including the first complete resolution of the G state fine structure in any atom [8]. Their experiments used a variation of the microwave-optical resonance technique in which the magnetic field was nulled to zero and the microwave frequency was varied. A review of these experiments and the techniques used to perform them can be found in Ref. [10]. The first precise measurements of the fine structure of high-L helium Rydberg states were performed in 1981 by Cok and Lundeen [11] using a fast beam microwave resonance technique in which the high-L states were detected through their cascading optical decay. The fast beam technique employed in the present experiments was initially used in measurements on high-L Rydberg states of helium by Palfrey and Lundeen [12], who detected $n=10$ helium Rydberg states in a fast atomic beam by selective laser excitation to $n\approx 30$ (n is the principal quantum number of the Rydberg electron), followed by Stark ionization of the high-n state. Later, Hessels *et al.* [13,14] used this technique to measure a range of high-L intervals in $n=10$ helium. A somewhat different technique has recently been used to measure $5F$-$5G$ intervals in helium [15].

The recent efforts to improve measurements of high-L helium Rydberg structure were stimulated in large part by the suggestion of Kelsey and Spruch that there could be significant contributions to the level structure from retardation effects [16]. They suggested that the structure of large atoms ($r\geq 137a_0$) would reflect retarded electromagnetic interactions related to the Casimir-Polder effect. Even though their approximate evaluation of the additional potential due to this effect,

$$V_{\mathrm{KS}}=\frac{11\alpha}{4\pi}\frac{\alpha_d}{r^5} \tag{1}$$

[where α_d is the adiabatic dipole polarizability of the $He^+(1s)$ core, α is the fine-structure constant, and r is the radial coordinate of the Rydberg electron], was later shown to be inadequate for states as small as the $n=10$ Rydberg states, their suggestion has proved to be a powerful stimulus for progress in this area.

A more detailed evaluation of the effects of retardation, appropriate for $n=10$ helium, was carried out in 1984 by Au, Feinberg, and Sucher [17] and later independently confirmed by Babb and Spruch [18]. Both of these

*Present address: Fresnel Technologies, Inc., 101 W. Morningside Drive, Fort Worth, TX 76110.

groups calculated the "retarded two-photon-exchange potential," the additional interaction between the Rydberg electron and the $He^+(1s)$ core not described by instantaneous Coulomb interactions.

The binding energies of the high-L helium Rydberg states, including only the instantaneous Coulomb interactions, were first calculated precisely by Drachman [19]. His approach depends explicitly on the spatial separation of the two helium electrons and results in an effective potential for the outer electron expressed as a series in increasing negative powers of that electron's radial coordinate. For a high-L electron, the convergence of this series is sufficiently rapid that a very precise result is obtained after including only the first few terms. Relativistic corrections have also been calculated in this approach [19,20]. A completely different approach has been taken by Drake [21]. He calculates the Coulomb wave functions and energies using a variational method that can be applied to any state of the helium atom. Using these wave functions, relativistic (Breit) and QED (one- and two-electron Lamb shift) corrections can also be calculated. Drake's results [21] are by far the most precise calculations to date for general singly excited states of helium, including high-L states. The two approaches yield precise predictions for the energies of the $n \leq 10$, $L=7$ states, which are in good agreement, confirming the accuracy of both calculations.

It is now well established that the retardation corrections calculated by Au, Feinberg, and Sucher [17] and later by Babb and Spruch [18] are essentially correct since experiments confirm that corrections to the instantaneous Coulomb energies of this magnitude and sign occur in nature [13,14]. The full correction, called $\langle V_{\rm ret} \rangle$, is applied directly as a correction to the calculations of Drachman. However, it has also been established that in the approach of Drake, the leading effects of retardation are implicitly included under other names, so that the net correction that needs to be applied to Drake's calculation is much smaller. In particular, most of the retardation effect is included through the spin-independent term in the Breit interaction and the "Q term" in the two-electron Lamb shift. The residual correction has been labeled $\langle V''_{\rm ret} \rangle$ and its presence signals the degree to which Drake's approach fails properly to include retardation. In smaller atoms, this correction is negligible. In much larger atoms, its significance increases. Retardation effects at the level of $\langle V''_{\rm ret} \rangle$ have not yet been confirmed by experiment and in fact theory and experiment presently disagree at this level.

The fine structure of the $n=10$ states of helium is shown in Fig. 1. The hydrogenic lifetimes of the states are shown beneath the labels for each state. The structure separating states of different L is given to first order by the shift of the Rydberg electron's energy due to the polarization of the $He^+(1s)$ core by the Rydberg electron,

$$\Delta E = -\frac{1}{2}\frac{e^2\alpha_d}{r^4}\ , \tag{2}$$

where e is the electron charge and the other symbols are defined as above. The finer level of structure indicated at the right of the figure is due primarily to spin-orbit and spin-spin interactions. We can see in the figure that the D states exhibit the familiar singlet-triplet structure, because there is significant overlap between the wave functions of the core and the Rydberg electrons. The higher-L manifolds, on the other hand, consist of four approximately equally spaced states. The exchange energies are very small for these states, so that the $J=L$ states are mixtures of singlet and triplet states and are labeled $^{+,-}L_L$. For the highest-L manifolds, the $J=L$ states are approximately equal mixtures of singlet and triplet states.

The high-precision variational calculations of Drake [21] are in close agreement with the $n=10$ experimental results, though there is a systematic discrepancy between the theory and the 10F-G, the G-H, the H-I, and the I-K measurements of Hessels *et al.* [13,14]. The previous

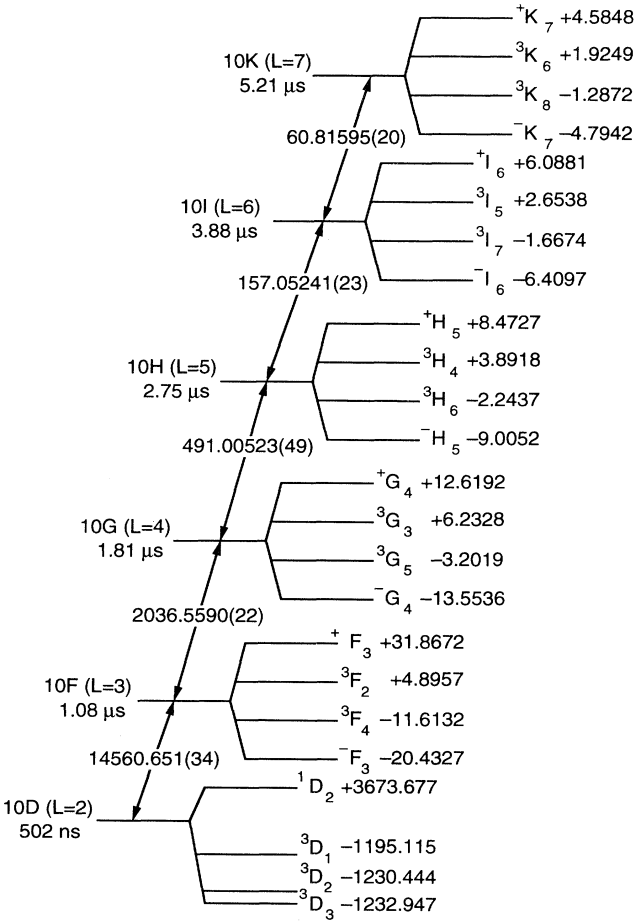

FIG. 1. Fine structure of the $n=10$ states of helium. (All energies are in MHz.) The spacing between manifolds of different L is due to the electrostatic interaction of the two electrons and to their exchange energy, while the much finer level of structure within each manifold is due primarily to spin-orbit and spin-spin interactions. The frequencies listed at the right of the figure are the offset of each state from the mean energy of the manifold. The spacings shown between the manifolds of different L are from the experiments of Hessels *et al.* [13,14] for the high-L intervals and of Farley, MacAdam, and Wing [9] for the 10D-10F interval. The spin structure shown in the figure is that calculated by Drake [21].

TABLE I. Comparison of experimental and theoretical mean energy intervals for the $n=10$ states of helium. All intervals are in MHz, with one standard deviation shown in parentheses. The theoretical values listed here include the small retardation correction V''_{ret} discussed in the text. The four high-L intervals may be seen to be consistent with a 6 ppm discrepancy with theory, while the 10*D*-10*F* interval agrees exactly.

Interval	Previous measurement	Theory[a] + V''_{ret}	$(E-T)/E$
I-K	60.815 95(20)[b]	60.816 471(14)	$-0.85(33)\times10^{-5}$
H-I	157.052 41(23)[b]	157.053 23(5)	$-0.52(15)\times10^{-5}$
G-H	491.005 23(49)[b]	491.007 51(7)	$-0.46(10)\times10^{-5}$
F-G	2 036.559 0(22)[c]	2 036.573 25(40)	$-0.70(11)\times10^{-5}$
D-F	14 560.651(34)[d]	14 560.652 3(18)	$-0.00(23)\times10^{-5}$

[a]Reference [21].
[b]Reference [14].
[c]Reference [13].
[d]Reference [9].

measurement by Farley *et al.* [9] of the mean *D-F* interval in $n=10$ helium agrees perfectly with the theory, albeit with a relatively larger error bar. The situation is shown in Table I, where the mean intervals derived from the measurements of Hessels *et al.* [13,14] and of Farley *et al.* [9] are compared with the theory of Drake [21]. The measurements of Hessels *et al.* [13,14] in the high-L states all disagree with theory by about 6 ppm (parts per 10^6), whereas the measurement by Farley, MacAdam, and Wing [9] of the 10*D-F* interval agrees exactly with theory and disagrees with the pattern observed at higher L by about two experimental standard deviations. This apparent break in the pattern of discrepancies between theory and experiment motivated the present measurements. We remeasured the 10*D-F* intervals to clarify whether or not the systematic discrepancy observed at higher L extends to the 10*D-F* interval.

II. EXPERIMENTAL TECHNIQUE

The experiment is performed using a fast atomic beam microwave resonance technique developed at Harvard and at Notre Dame over the past 15 years [1,12–14,22]. The experiment relies on three basic techniques: the production of a fast beam of neutral Rydberg atoms through the collisional neutralization of positive ions produced by a small accelerator; excitation of microwave resonances in a hollow waveguide along the axis of which the fast atomic beam travels; and the selective detection of particular Rydberg state populations through a resonant laser excitation and Stark ionization scheme.

A schematic diagram of the experimental apparatus is shown in Fig. 2. A beam of 11-keV He^+ ions is produced and focused by a duoplasmatron ion source at 1 in Fig. 2. These ions are deflected into the main beam line and further focused by the bending magnet and ion optics at 2. Some of the ions are neutralized in an argon-gas-filled charge exchange cell at 3, where the remaining ions are deflected out of the beam by a pair of electrostatic deflection plates and therefore do not pass through the collimating slits. The collisional neutralization results in a very broad distribution of excited states of the captured electron. Some small fraction of the collisionally neutralized atoms are in $n=10$ states, and this small fraction contains the atoms that we study in this experiment. The beam also contains, after the collisional neutralization, some atoms in high-n Rydberg states. Atoms with $n \geq 17$ are Stark ionized and electrostatically removed from the beam immediately after the charge exchange cell at 3 in the figure, since they would otherwise contribute to background in the detector.

The CO_2 laser interaction regions at 4 and 6 in the figure are Doppler tuned to excite various resonances between $n=10$ and 31. Doppler tuning is accomplished by changing the intersection angle between the laser beam and the fast atomic beam. With a fast beam of $v/c \geq 0.001$, Doppler tuning combined with the selection of several discrete CO_2 laser lines (spacing approximately equal to 1 cm^{-1}) gives continuous frequency coverage near 10 μm.

In our detection scheme, the CO_2 laser-excited $n=31$ atoms are Stark ionized in an electric field of $\sim$2300 V/cm, directed along the beam axis, which ionizes states with $n \geq 20$. The resulting ions are electrostatically deflected into a channeltron electron multipler (CEM) and collected. The Stark ionizer and detector used in these experiments are very similar to those used by Hessels *et al.* [13,14]. Details of their construction, as well as details of the rest of the experimental apparatus, may be found in Ref. [23].

A Doppler-tuned spectrum of the high-L helium $n=10$–31 excitations is shown in Fig. 3. The spectrum

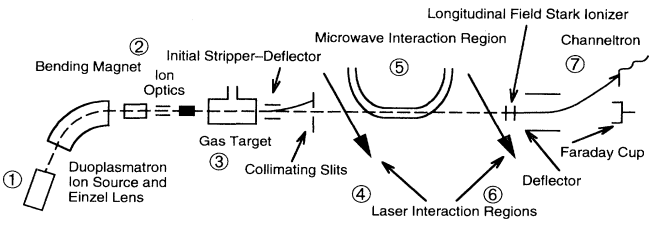

FIG. 2. Schematic diagram of the experimental apparatus. The main components of the apparatus are the duoplasmatron ion source at 1, the gas neutralization cell at 3, the CO_2 laser interaction regions at 4 and at 6, the microwave interaction region at 5, and the Stark ionizer and detector at 7.

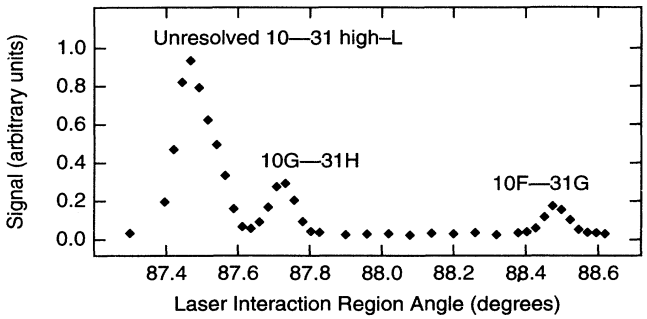

FIG. 3. Doppler-tuned scan of some $n=10-31$ resonances in the laser interaction region shown at 6 in Fig. 2. As the angle between the fast atomic beam and a grating-tuned CO_2 laser beam is changed, the Doppler effect allows various $n=10-31$ transitions to be excited. The transition labeled $10F$-$31G$ is used in this experiment to detect the population of the $10F$ manifold.

in the figure represents the component of the ion current in the CEM synchronous with the 100% amplitude modulation of a CO_2 laser, grating tuned to the $R(32)$ line of the 10.4-μm band at 983.252 cm^{-1}. The resonances in the spectrum are identified with the transitions (right to left) $10F$-$31G$, $10G$-$31H$, and several unresolved higher-L transitions in the 10-31 manifold.

The microwave interaction region at 5 in Fig. 2 is inserted between the laser interaction regions in order to perform our microwave resonance experiments. The microwave region consisted of a straight section of P-band waveguide (inside dimensions: 1.560 cm×0.780 cm) between two bends. The microwave region was shielded from the Earth's magnetic field by two unannealed layers of μ-metal shielding, which reduced the transverse magnetic field to ≤ 20 mG and the axial magnetic field to ≤ 50 mG everywhere inside the microwave region. The waveguide bends are in the plane of the long dimension of the waveguide, so that the microwave electric field is always perpendicular to the direction of the atomic beam. There is a small hole in each bend that allows the atomic beam to pass through; a small tube (4 mm inner diameter ×4.5 cm length) is attached at each hole in order to prevent leakage of microwaves from the region. The microwave interaction region used in these experiments is made from a single length of brass, with no joints between the straight section and the bends. Constructing the region of a single metal reduces contact potentials, which lead to stray dc electric fields inside the interaction region. Because cleaning is a critical step in the reduction of stray dc electric fields, the top of this region is removable so that the inside may easily be cleaned. The region was heated to a temperature of approximately 90 °C at all times during the experiments. Cleaning and heating the region dramatically reduced the size of stray dc electric fields inside the microwave interaction region, apparently by preventing the buildup of nonconducting residues on the inner surfaces of the waveguide. Data acquisition was interrupted whenever the heater was turned on, due to the large magnetic field produced by the current in the heater coil.

The microwaves were generated by a Hewlett-Packard 8673C frequency synthesizer and were 100% amplitude modulated. The output of the synthesizer was attached to a 3-dB attenuator and was carried to the experimental apparatus by about 7 m of P-band waveguide, including some flexible sections. The microwave power transmitted through the region was measured using a Hewlett-Packard 435B power meter with either a Hewlett-Packard 8481A or 8481D power sensor.

The purpose of each piece of equipment described above will be made clearer by a description of a specific experiment performed using this apparatus: measurement of the $10\,^3D_3-{}^3F_4$ resonance frequency. Among the atoms that have captured electrons into $n=10$ Rydberg states, the various fine-structure states of different L are roughly equally populated. In the upstream laser interaction region, the atoms with their Rydberg electron in any state of the $10\,^3D$ manifold are excited to the $31F$ state. This excitation enhances the population difference between the $10\,^3D$ and the $10\,^3F$ states. The transition from $10\,^3F_4$ to $10\,^3D_3$ is then resonantly driven in the microwave region. Finally, in the downstream laser interaction region the laser is used to excite the $10F$-$31G$ transition. The $31G$ atoms are Stark ionized and deflected into the channeltron detector and the ion current synchro-

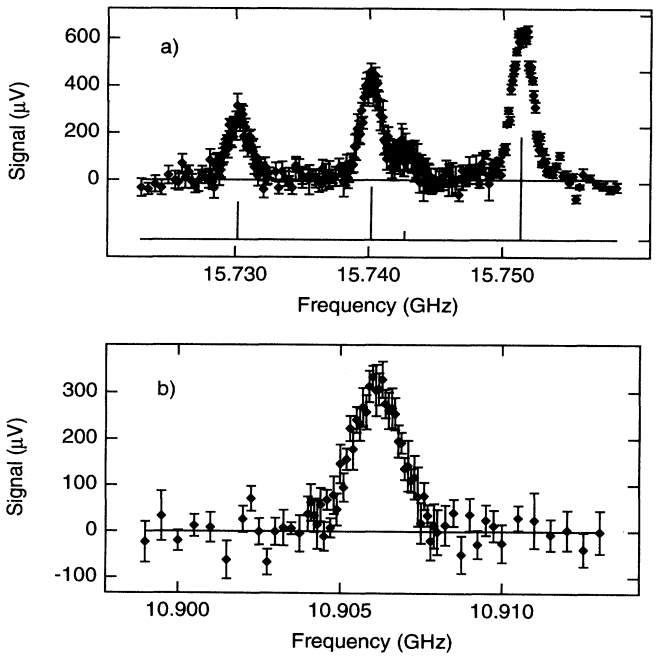

FIG. 4. Representative data from this experiment, taken with the microwaves propagating antiparallel to the fast atomic beam. (a) shows the triplet resonances (left to right) $10\,^3D_1-{}^3F_2$, $10\,^3D_2-{}^-F_3$, $10\,^3D_3-{}^-F_3$, and $10\,^3D_3-{}^3F_4$. The $10\,^3D_3-{}^-F_3$ resonance is a small shoulder on the high-frequency side of the $10\,^3D_2-{}^-F_3$ peak. Also shown is a stick diagram indicating the expected positions and relative intensities of the resonances. The heights of the sticks are proportional to the square of the dipole matrix element and to the number of magnetic substrates for each resonance. (b) shows the singlet resonance $10\,^1D_2-{}^+F_3$, which occurs 4.8 GHz below the triplet resonances.

nous with 100% amplitude modulation of the microwaves is taken as the signal. Representative signals from this sort of experiment are shown in Fig. 4. The synchronous ion current is proportional to the population of the 31*G* manifold, and since atoms are removed from the state excited in the second laser interaction region when the microwave frequency is resonant with the transition under study, the microwave resonance causes a decrease in the detected ion current. This decrease is taken to be a positive signal.

The data for this experiment were taken in two independent runs, the results of which were then averaged together to obtain the final results for the measured intervals. Each resonance measurement consists of data points taken at frequencies scattered more or less symmetrically about the center frequency of the resonance. The points were not taken in linear order, but rather the scanning program jumped back and forth symmetrically across the resonance peak. This scheme tends to minimize the effects of changes in signal size during the scan. Since the observed resonances are strongly Doppler shifted, each transition was measured for both directions of microwave propagation through the waveguide relative to the beam and each of these resonances was separately fitted to determine its center. The pairs of line centers were then averaged in order to determine the frequency intervals for a stationary atom.

III. STRAY dc ELECTRIC-FIELD DIAGNOSTIC METHODS

The major experimental difficulty in these measurements was in the elimination of shifts due to the effects of stray dc electric fields in the microwave interaction region. dc electric fields cause substantial Stark shifts [≈ 2 MHz/(V/cm)^2] in the 10*D*-10*F* line centers, so that we must eliminate these fields to the greatest degree possible and characterize the shape and the magnitude of those remaining in order to correct the line centers for the residual Stark shifts. The size of the stray dc electric fields was greatly reduced by heating and thorough cleaning of the microwave interaction region.

Two different diagnostic methods were developed for determining the size and the spatial extent of stray dc electric fields inside our waveguide interaction region. The first, which is quite analogous to the method used by Hessels *et al.* [14] to measure the stray fields in a transmission line interaction region, involves measuring the positions of the lines in the $29\,^3P-29\,^3D$ manifold. Since the ratio of the Stark shift rates of the $29\,^3P-29\,^3D$ intervals to those of the 10*D*-10*F* intervals is very large and well known, the Stark shifts of the 10*D*-10*F* intervals under study may be extracted quite accurately from the Stark shifts of the $29\,^3P-29\,^3D$ intervals. The $29\,^3P-29\,^3D$ transitions were chosen because they can be driven in a *P*-band waveguide and because accurate zero-field energies for these intervals can be obtained by extrapolating Drake's calculations of the lower-*n* *P*-*D* intervals [21,24]. This method is more sensitive to stray fields occurring over large portions of the waveguide interaction region than it is to large stray fields occurring for a relatively small portion of the interaction region. This fact provides the impetus for the development of a second stray electric-field diagnostic method.

The second method involves measuring Stark-assisted 10*D*-10*G* single-photon transitions. These transitions are forbidden in the absence of dc electric fields. In the presence of a dc electric field, however, the *F* and *G* states are slightly mixed, allowing single-photon transitions between the *D* and the *G* states. The Stark-assisted diagnostic method has the advantage of not requiring accurate calculations or previous measurements of the intervals in question, since one does not measure frequency shifts in this technique. This technique may therefore be applicable to other systems for which accurate high-*n* energies are unavailable. The results obtained from the two methods will be compared.

The $29\,^3P-29\,^3D$ transitions are observed as follows: the $10\,^3P-29D$ transition is driven in the first laser interaction region, transferring some population into the 29*D* manifold. Then a $29\,^3P-29\,^3D$ transition, say, the $29\,^3P_2-29\,^3D_3$ transition, is driven in the microwave interaction region, transferring some of the $29\,^3D_3$ population to the $29\,^3P_2$ state. As the atoms travel between the two laser interaction regions, any population remaining in the $10\,^3P$ manifold after the first laser interaction region decays into lower-*n* states. Finally, in the second laser interaction region, the $10\,^3P-29D$ transition is again driven. But in the second laser interaction region this transition transfers population down to the (now nearly empty) $10\,^3P$ manifold, where it cannot be Stark ionized in the detector. Since the microwave resonance transfers population to a state that is not transferred to $n=10$ in the second laser interaction region, the resonance corresponds to an increase in the detected ion current. Thus these resonances have a negative sign relative to the 10*D*-10*F* resonances.

A representative scan of the microwave resonance used in this diagnostic is shown in Fig. 5. In this scan, we can see that the resonance consists of a main portion at 17.681 GHz, which is somewhat broader (compare with Fig. 4, for instance) than would be indicated by the transit time, as well as a shoulder on the low-frequency side of the resonance. Our modeling of Stark-broadened line shapes show that the peak and shoulder cannot be produced by a constant stray dc electric field for the entire length of the microwave interaction region. We therefore postulate the next-simplest field configuration, which is two regions with different stray dc electric fields. The presence of different-sized fields seems physically reasonable since there may be regions of waveguide that are not as well cleaned or there might be a region of waveguide where the beam passes closer to the wall of the waveguide than it does elsewhere. We might think, for instance, of the beam grazing the interaction region walls mostly near the downstream hole in the waveguide. In our simple model, the boundary between the regions is sharp and the sum of their lengths is equal to the total length of the microwave interaction region, as shown in Fig. 6. In both regions the stray electric field is taken to be purely along the short dimension of the waveguide.

The line shape in the presence of this field configuration was calculated using evolution operators to prop-

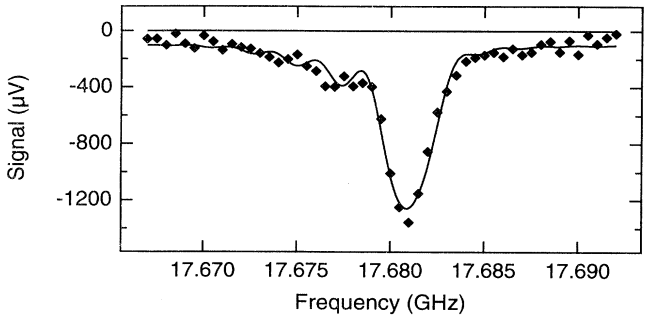

FIG. 5. Experimental data and the results of a fit for the $29\,^3P-29\,^3D$ stray dc electric-field diagnostic. The resonance may be seen to consist of a main portion at about 17.681 GHz, with a prominent shoulder on the low-frequency side. The fit line shown in the figure is the complete line shape within the simple model discussed in the text, including the interference terms between the amplitudes from the two field regions. These interference terms are strongest in the frequency region between the main peak and the low-frequency shoulder. The oscillations in that area are nearly removed by ignoring the interference terms in the fit and the results obtained for the stray electric-field parameters when the interference terms are ignored agree closely with those obtained from the full line shape. The stray field parameters listed in Table III are derived from an average of the fits with and without the interference terms.

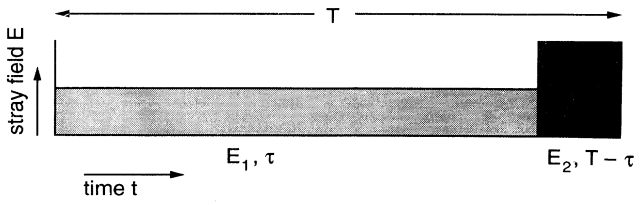

FIG. 6. Stray electric-field configuration modeled in this work, showing the parameters E_1, E_2, T, and τ discussed in the text and listed in Table III.

agate the (two-level) atom through the two field regions. We assume that the stray electric field is parallel to the microwave field and therefore does not mix the m states. We further assume that the m states are equally populated at the entrance to the interaction region and add the contribution from each m state. (The assumption of equally populated m states leads to insignificant uncertainty in the derived $10D$-$10F$ Stark shifts.) This procedure yields a line shape that resembles that observed in the experiments, as shown by the fitted line in Fig. 5.

The zero-field positions of the $29\,^3P-29\,^3D$ lines may be extrapolated from the extremely accurate lower-n variational calculations of Drake [21]. He has in fact performed the fits necessary for this extrapolation [24] and the results are listed in Table II, along with the hydrogenic matrix elements of z and the Stark shift rates of interest. We fit the experimentally observed resonances to the line-shape discussed above, including the superposition of all eight transitions. The parameters of the fit are the two electric fields and the length of the region of smaller field (E_1, E_2, and τ, as shown in Fig. 6), along with an overall amplitude and an offset from zero. The results of one such fit are shown in Fig. 5. The stray electric-field parameters extracted from this fit are $E_1=76(1)$ mV/cm, $E_2=112(5)$ mV/cm, and $\tau=0.364(12)$ μs, indicating the presence of a 112-mV/cm field for one-quarter of the length of the region and a 76-mV/cm field for the remainder of the 0.480 μs spent in the region.

The oscillations in the model line shape between the main peak and the shoulder in Fig. 5 are due to interference between the amplitudes from the two field regions. The interference is strongest when the fields are assumed to turn on and off suddenly, as in the model discussed here. However, fits to a line shape with no interference terms gave very similar results for the fitted field parameters. The stray fields and the lengths obtained from the fits to experimental resonances are listed in Table III, along with the rms stray fields calculated from the parameters listed in the table. The average rms stray field was 78(6) mV/cm for run 1 and 89(5) mV/cm for run 2.

A simpler way to extract the rms stray field from the $29\,^3P-^3D$ diagnostic is to examine the center of gravity of the resonance, including the shoulder. The position of the center of gravity should be Stark shifted by $kE_{\rm rms}^2$, where k is the average Stark shift rate of the $29\,^3P-29\,^3D$ transitions and $E_{\rm rms}$ is the rms stray field in the region. This model, which does not depend on the simplifying assumption of a two-component field, gives results consistent with our more complicated modeling.

A second diagnostic method using the Stark-assisted $10D$-$10G$ transitions leads to an independent measure of the stray electric fields present in the microwave interaction region. These $\Delta L=2$ transitions are seen only in the presence of dc electric fields. The width of the Stark-assisted resonances gives information about the transit

TABLE II. Zero-field positions as extrapolated from Drake [21,24], matrix elements, and Stark shift rates for the $29\,^3P-29\,^3D$ transitions.

Transition	m	Zero-field center (MHz)	$\Delta\nu_{DF}$ (MHz)	z matrix element (a_0)	Stark shift rate [MHz/(V/cm)^2]
$29\,^3P_1-^3D_2$	0	17 720.569	657.436	563	−626
	±1			487	−470
$29\,^3P_2-^3D_3$	0	17 721.125	657.872	617	−751
	±1			581	−668
	±2			460	−417

TABLE III. Stray dc electric-field parameters from the $29\,^3P-29\,^3D$ diagnostic method. The parameters shown in the table are averages of the results of fits to the diagnostic data for each run. The parameters are the two fields E_1 and E_2 and the duration τ shown in Fig. 6. The rms field calculated from these is shown in the last column.

Run	E_1 (mV/cm)	E_2 (mV/cm)	τ (μs)	$E_{\rm rms}$
1	71(5)	95(4)	0.350(40)	78(6)
2	79(3)	112(6)	0.349(11)	89(5)

time of the atoms through the stray field and the size of the signal gives an indication of the magnitude of that field, since the Stark coupling matrix element is proportional to the stray electric field. This resonance was observed during one of the data runs as a test of the $29\,^3P-29\,^3D$ field diagnostic.

The 10D-10G coupling is due to effective matrix elements, which are products of matrix elements due to the dc electric field and matrix elements due to the microwave field, divided by the energy defect. The coupling is given by

$$V_{DG}=\left[\frac{ez_{DF}E_{\rm rf}}{2h}\right]\left[\frac{ez_{FG}E_{\rm dc}^{\rm stray}}{h}\right]\frac{1}{\Delta}\ , \tag{3}$$

where Δ is the 10F-10G frequency interval for the transition in question, z_{FG} is the dipole matrix element between the Stark-coupled F and G states, z_{DF} is the 10D-10F dipole matrix element, $E_{\rm rf}$ is the microwave electric field, and $E_{\rm dc}^{\rm stray}$ is the stray dc electric field in the region under study.

The 10D-10G resonances are significantly ac Stark shifted; this shift is due primarily to the off-resonant coupling between the 10D and the 10F manifolds caused by the large microwave power present in the interaction region during these diagnostic runs. The ac Stark shift is given by [25]

$$\Delta\nu_{\rm ac}=\left|\frac{ez_{DF}E_{\rm rf}}{2h}\right|^2\frac{1}{\Delta} \tag{4}$$

and shifts the 10D-10G resonances toward lower frequency. The shifts are as large as 10 MHz. The dc Stark shifts of these resonances are much smaller and may be ignored.

We observed the $10\,^3D-10\,^3G$ resonances (at 10 mW microwave power) and the $10\,^3D_3-{}^3F_4$ resonance (at 42 nW microwave power). Both resonances were detected with the same laser transition ($10\,^3D-31F$) driven in regions 4 and 6 shown in Fig. 2 and the same detector settings. Both resonances were also modeled in an evolution operator framework. The experimentally observed $10\,^3D-10\,^3G$ signals are given by the product of the initial population difference, the transition probability, and the detection efficiency. The simulations calculate the transition probabilities for both the $10\,^3D-10\,^3G$ and the $10\,^3D_3-{}^3F_4$ transitions, which, in the case of the $10\,^3D-10\,^3G$ transitions, depend on the stray fields. The detection efficiency should be the same for both resonances because the $10\,^3D$ state is detected in both cases. The initial population difference should be about a factor of 2 larger for the $10\,^3D-10\,^3G$ resonance because of the longer lifetime of the 10G state. Taking this factor into account and normalizing to the size of the observed $10\,^3D_3-{}^3F_4$ resonance, the simulation predicts both the size and the shape of the $10\,^3D-10\,^3G$ signal under various conditions of stray field.

The data were fitted with the model discussed above, varying the parameters E_1, E_2, and τ in the assumed simplified dc electric field shown in Fig. 6. There was some difficulty in fitting a reasonable zero offset to the available data, so the zero offset was set to -5 μV and was not varied. The results of this fit are shown in Fig. 7. The parameters determined by the fit are $E_1=72(3)$ mV/cm, $E_2=398(87)$ mV/cm, and $\tau=0.471(2)$ μs, indicating a field of about 400 mV/cm for 9 ns and a field of 72 mV/cm for the remaining 471 ns. The rms electric field implied by this stray field configuration is 89(14) mV/cm, which is about 15% larger than (but in agreement with) that obtained from the $29\,^3P-29\,^3D$ diagnostic during the same run. Although these measurements are not as accurate as the $29\,^3P-29\,^3D$ field determinations, they do form an independent measure of the field size and, in particular, test for the presence of large dc fields that act for short times. The $29\,^3P-29\,^3D$ diagnostic is relatively insensitive to these large, localized fields. The shortest physically reasonable distance scale for such fields is 7 mm (the size of the waveguide), which corresponds to 10 ns. The analysis of the 10D-10G data indicates that fields of this duration must be less than 500 mV/cm.

Using the information about the stray dc electric fields derived from the two diagnostics, the resulting shifts in the 10D-10F resonances can be deduced. We make the assumption, valid for Stark shifts small relative to the resonance linewidth, that the 10D-10F Stark shift is given by

$$\Delta\nu_{\rm Stark}=k_{DF}E_{\rm rms}^2\ , \tag{5}$$

where the shift rate k_{DF} is given, in the approximation where the shift of the D state is taken to be negligible, by

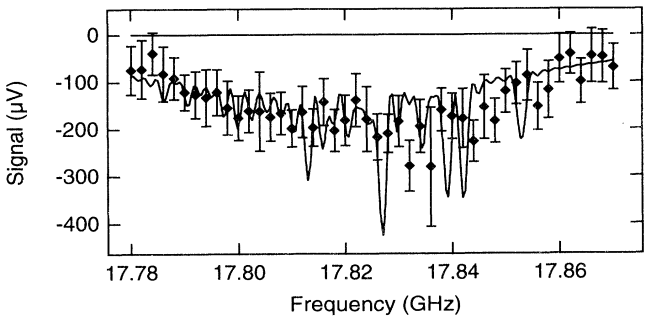

FIG. 7. Experimental data and results of a fit to the 10D-10G Stark-assisted diagnostic. The fit line shown is the complete line shape within our simple model of the stray dc electric field in the region. The data provide little evidence of the significant structure shown in the fit, but the data do provide evidence of a possible strong field acting for a very short time. This diagnostic is more sensitive to short, strong fields than is the $29\,^3P-{}^3D$ diagnostic.

$$k_{DF}=-\frac{1.3|\langle z_{FG}\rangle|^2}{\Delta_{FG}}=2.2\ \text{MHz}/(\text{V/cm})^2\ . \quad (6)$$

In this expression, $\langle z_{FG}\rangle$ is the rms matrix element of z (in MHz) between the F and the G states and Δ_{FG} is the energy difference (in MHz) between those same two states.

From the two diagnostics, our best estimate of the rms stray field is $E_{\text{rms}}=85$ mV/cm, with no indication of any variation of the field with time. This produces a Stark shift of about -16 kHz in the $10D$-$10F$ resonances. Taking into account the limits set by the $10D$-$10G$ diagnostic on possible intense fields of short duration, we estimate the uncertainty in this determination to be 50% of the shift.

IV. MEASUREMENTS

The four intervals measured in this work are $10\,^1D_2-{}^+F_3$, $10\,^3D_1-{}^3F_2$, $10\,^3D_2-{}^-F_3$, and $10\,^3D_3-{}^3F_4$. The data were collected in two completely independent runs, separated in time by a few days. Measurements of the stray electric fields in the microwave interaction region as described in the preceding section were interspersed with the $10D$-$10F$ resonance scans in order to monitor the stray electric fields during the entire course of the experiments. These two "runs" provide two independent determinations of each line center.

All four intervals were measured with the microwaves propagating both parallel and antiparallel to the atomic beam so that the Doppler shifts due to the atomic beam velocity could be averaged out. Data showing the relative positions of the observed $10\,^3D-10F$ resonances are presented in Fig. 4(a). The data shown in the figure are uncorrected for Doppler shifts (as well as for any other effects); the lines shown are, left to right, $10\,^3D_1-{}^3F_2$, $10\,^3D_2-{}^-F_3$, $10\,^3D_3-{}^-F_3$, and $10\,^3D_3-{}^3F_4$. Note that $10\,^3D_3-{}^-F_3$ is much weaker than the other three lines and only partially resolved from $10\,^3D_2-{}^-F_3$. Also shown in the figure is a stick diagram indicating the predicted positions of the lines and their predicted relative weights, taking into account both the dipole matrix elements and the statistical weights of the various states involved. The $10\,^1D_2-{}^+F_3$ resonance occurs approximately 4.8 GHz below the $10\,^3D-10F$ resonances and is shown in Fig. 4(b).

A line center was extracted from each resonance scan by a least-squares fit of the data to the expression

$$S(\nu)=AV^2\left[\frac{\sin bT}{bT}\right]^2, \quad (7)$$

where S is the signal at a given frequency ν, A is the amplitude of the resonance, V is the $10D$-$10F$ matrix element, and b is given by

$$b=[\pi^2(\nu-\nu_0)^2+V^2]^{1/2}\ . \quad (8)$$

The parameters of the least-squares fit were the amplitude A, the line center ν_0, and the transit time T, as well as a small zero offset. The fitted line shape does not include possible effects due to the nonsudden turn on of the field in the bend regions of the waveguide or of the varying Doppler shift in the bend regions. Nevertheless, this line shape was adequate for these fits where the line center was determined only to about 1% of the linewidth. The fits were relatively insensitive to the value of the transition matrix elements, so these were held to their calculated values of approximately 0.45 MHz. The fits returned values of the transit time of about 0.45 μs, consistent with the expected value.

The $10\,^3D_2-{}^-F_3$ resonances had to be dealt with somewhat differently from the rest of the scans. The difficulty with fitting these scans using the procedure described above is that the $10\,^3D_3-{}^-F_3$ resonance appears as a small shoulder on the high-frequency side of the $10\,^3D_2-{}^-F_3$ resonance. We did not try to determine the line center for the $10\,^3D_3-{}^-F_3$ resonance, but we had to account for the effect of this small shoulder on the $10\,^3D_2-{}^-F_3$ line shape if we expected to make an accurate determination of the $10\,^3D_2-{}^-F_3$ line center. The scheme chosen was as follows. These scans were fitted to a pair of lines. The overall amplitude of the resonance was allowed to float, as was the transit time. The relative amplitude of the two resonances was constrained as in the single-line line shape formula, to be in proportion to the squares of their rms matrix elements, and the two resonances were weighted according to the number of m states involved in each resonance. The separation between the peaks was set to its theoretical [21] value of 2.515 MHz. The fitted values of the line centers were not changed significantly by varying the separation of the two lines by as much as 0.3 MHz or by allowing the relative amplitude to vary with the separation held fixed.

The results of all the fits discussed above are presented in Table IV. The results presented are those returned by the fits with the matrix element V for each transition held to its calculated value; in the case of the $10\,^3D_2-{}^-F_3$ resonances the separation of the two lines was held fixed along with the matrix elements. Two results listed in Table IV require a bit more discussion. The copropagating $10\,^1D_2-{}^+F_3$ resonance in run 1 had an extremely poor signal-to-noise ratio and the fit returned a transit time that was much too long. Thus the transit time was constrained to 0.437 μs (the average of the other two transit times for the singlet resonances in run 1) and the scan was refitted to obtain the result listed in the table. Even then, however, this fit had an exceptionally large χ^2 and as a result this resonance is not used in the determination of the final line center for the $10\,^1D_2-{}^+F_3$ resonance; this result is marked in the table with an asterisk to indicate that it is not used. The counterpropagating $10\,^1D_2-{}^+F_3$ resonance frequency was simply not measured in run 2. Consequently, only one of the copropagating and counterpropagating resonance frequencies for the $10\,^1D_2-{}^+F_3$ transition was measured in each run. However, we may apply the knowledge of the Doppler shift obtained from the other resonances in order individually to correct the three measurements of the $10\,^1D_2-{}^+F_3$ line center and so to obtain three independent determinations of the stationary-atom $10\,^1D_2-{}^+F_3$ line center.

TABLE IV. Results of fits to resonance scans. The asterisk next to the copropagating scan of the $10\,^1D_2-{}^+F_3$ resonance in run 1 indicates that the fit to that scan was not used in the analysis because of a considerably worse signal to noise for that one scan.

Interval	Propagation direction	Line center (MHz)	Transit time (μs)
	Run 1		
$10\,^3D_3-{}^3F_4$	copropagating	15 812.612(14)	0.454(6)
$10\,^3D_3-{}^3F_4$	counterpropagating	15 751.404(15)	0.442(7)
$10\,^3D_2-{}^-F_3$	copropagating	15 801.273(20)	0.460(10)
$10\,^3D_2-{}^-F_3$	counterpropagating	15 740.198(42)	0.404(17)
$10\,^3D_1-{}^3F_2$	copropagating	15 791.270(41)	0.432(17)
$10\,^3D_1-{}^3F_2$	counterpropagating	15 730.089(31)	0.434(15)
$10\,^1D_2-{}^+F_3$	copropagating*	10 931.459(61)	0.437(held)
$10\,^1D_2-{}^+F_3$	counterpropagating	10 906.139(28)	0.459(10)
$10\,^1D_2-{}^+F_3$	counterpropagating	10 906.109(30)	0.415(10)
	Run 2		
$10\,^3D_3-{}^3F_4$	copropagating	15 812.644(17)	0.441(9)
$10\,^3D_3-{}^3F_4$	counterpropagating	15 751.427(16)	0.443(6)
$10\,^3D_2-{}^-F_3$	copropagating	15 801.318(27)	0.430(11)
$10\,^3D_2-{}^-F_3$	copropagating	15 801.275(23)	0.446(8)
$10\,^3D_2-{}^-F_3$	counterpropagating	15 740.169(22)	0.468(9)
$10\,^3D_2-{}^-F_3$	counterpropagating	15 740.172(20)	0.465(7)
$10\,^3D_1-{}^3F_2$	copropagating	15 791.250(30)	0.457(13)
$10\,^3D_1-{}^3F_2$	copropagating	15 791.231(37)	0.441(17)
$10\,^3D_1-{}^3F_2$	counterpropagating	15 730.199(24)	0.449(11)
$10\,^3D_1-{}^3F_2$	counterpropagating	15 730.180(35)	0.406(15)
$10\,^1D_2-{}^+F_3$	copropagating	10 931.553(32)	0.439(11)

A number of corrections must be made to these raw data in order to extract the energy intervals for stationary atoms. The single largest correction to the measured frequencies is the correction for the Doppler shift of each interval. The Doppler shifted frequencies $\nu^{\pm}$ for resonances measured in a waveguide are given by

$$\nu_0=\gamma\nu^{\pm}\left[1\mp f_B\beta\left[\frac{\lambda_0}{\lambda_g}\right]\right], \tag{9}$$

where f_B is a numerical factor intended to take into account the effects of the waveguide bends on the Doppler shift, $\gamma=1/\sqrt{1-\beta^2}$, and

$$\frac{\lambda_0}{\lambda_g}=\left[1-\left[\frac{\nu_c}{\nu}\right]^2\right]^{1/2}. \tag{10}$$

A TE_{10} mode in a rectangular waveguide of long dimension $a=1.56$ cm has a cutoff frequency $\nu_c=9609$ MHz.

The parameter f_B is approximately equal to one and allows us to take account of the fact that the waveguide is not just a straight section, but also incorporates bends that allow the microwaves to be introduced along the atomic beam axis. In the limit where the straight section of the waveguide is much longer than the length of the bends, f_B is equal to one. f_B may be calculated in a simple model where the average Doppler shift is calculated by integrating the Doppler shift at each point in the waveguide weighted by the intensity of the microwave electric field at that point and dividing by the integrated microwave electric field intensity over the entire length of the waveguide interaction region. Following the treatment used elsewhere [26], for the geometry of our apparatus this calculation predicts $f_B=0.997$. Since we do not know the beam velocity to better than 0.3%, it is sufficient to take $f_B=1.000$ in this analysis. We may then solve for β and ν_0 in the Doppler shift equation; we find

$$\beta\cong\frac{\nu^+-\nu^-}{2\bar{\nu}f_B\lambda_0/\lambda_g|_{\bar{\nu}}} \tag{11}$$

and

$$\nu_0\cong\bar{\nu}[1+\beta^2(\tfrac{1}{2}-f_B^2)+O(\beta^4)], \tag{12}$$

with $\bar{\nu}\equiv(\nu^++\nu^-)/2$. The neglected correction of order β^4 is much less than 1 kHz, as is the change in the correc-

TABLE V. Uncorrected stationary-atom transition frequencies.

Interval	Averaged frequency (MHz)	Beam velocity β
	Run 1	
$10\,^3D_3-{}^3F_4$	15 781.961(10)	0.002 444 4(10)
$10\,^3D_2-{}^-F_3$	15 770.689(23)	0.002 441 6(20)
$10\,^3D_1-{}^3F_2$	15 760.633(26)	0.002 448 4(18)
$10\,^1D_2-{}^+F_3$	10 918.768(38)	
	Run 2	
$10\,^3D_3-{}^3F_4$	15 781.989(12)	0.002 444 8(10)
$10\,^3D_2-{}^-F_3$	15 770.687(12)	0.002 444 0(12)
$10\,^3D_1-{}^3F_2$	15 760.669(16)	0.002 443 6(12)
$10\,^1D_2-{}^+F_3$	10 918.849(60)	

TABLE VI. Correction of fitted intervals to obtain final results (in MHz). The Stark shift corrections can be seen to be the only corrections of any consequence, but the other potential systematic corrections discussed in the text are included for completeness.

Description	$10\,^3D_3-{}^3F_4$	$10\,^3D_2-{}^-F_3$	$10\,^3D_1-{}^3F_2$	$10\,^1D_2-{}^+F_3$
run 1	15 781.961(10)	15 770.689(23)	15 760.633(26)	10 918.768(38)
run 2	15 781.989(12)	15 770.687(12)	15 760.669(16)	10 918.849(60)
average	15 781.975(8)	15 770.688(13)	15 760.651(15)	10 918.808(36)
Stark shift	0.016(8)	0.016(8)	0.016(8)	0.016(8)
total	15 781.991(11)	15 770.704(15)	15 760.667(17)	10 918.824(37)
Other effects				
reflections	0.0004(8)	0.0002(4)	0.0003(6)	0.0016(32)
ac Stark	0.000(0)	0.000(0)	0.000(0)	0.000(0)
blackbody	0.000(0)	0.000(0)	0.000(0)	0.000(0)
power	0.000(1)	0.000(1)	0.000(1)	0.000(1)
time base	0.000(3)	0.000(3)	0.000(3)	0.000(2)
final result	15 781.991(11)	15 770.704(15)	15 760.667(17)	10 918.826(37)

tion of order β^2 due to the approximation $f_B = 1.000$.

Most of the results listed in Table IV can simply be averaged in this way. The results of averaging the individual line centers are presented in Table V. However, in the case of the singlet interval this averaging is not possible. In this case the resonance was measured in only one of the two directions of propagation during each run and so both numbers are not available for the averaging process discussed above. The singlet results presented in Table V are derived by correcting the individual fitted line centers for the Doppler shift, with β taken to be 0.002 444 8(14) for run 1 and 0.002 444 1(7) for run 2. The average beam velocities derived from the data taken on two different days are in agreement to better than 3 parts in 10^4, so it seems clear that β does not change significantly during a single run.

Several corrections must be applied to each of the intervals listed in Table V in order to find the correct frequency for a completely unperturbed atom. The most important of these corrections is the correction for the dc Stark shift. The other possible corrections to the measured intervals include corrections due to the ac Stark shift, corrections due to the fact that the atoms are bathed in a sea of 360 K blackbody radiation [27] during their interaction with the microwave field, and corrections due to microwave reflections. All corrections other than the dc Stark shift corrections are found to be insignificant at the level of the statistical uncertainties in our measurements.

A final uncertainty is in the calibration of the time base of the frequency synthesizer. The Hewlett-Packard 8673C generator with option H41 (high stability time base) used in this work is specified to have time base stability of 0.1 ppm/yr and 2.5×10^{-9} over 0–71 °C. The frequency of this synthesized generator was compared at 10 MHz (the frequency of the internal standard) to a less than 1-yr-old Hewlett-Packard 83640A synthesized generator with similar specifications. The time bases were observed on two separate occasions to differ by no more than 0.1 ppm. We conclude, therefore, that a conservative treatment of the uncertainty due to time base calibration allows 0.2 ppm additional uncertainty in each interval due to this effect.

We obtain the final results for the four intervals measured here by correcting for Stark shifts and for the other effects listed above. This process is shown in Table VI, where it is evident that the uncertainties in the final results come about equally from the statistical uncertainty in fitting the line centers and from the uncertainty in the Stark shift correction to each interval.

TABLE VII. Results of this work compared with the previous work of Farley, MacAdam, and Wing [9]. All values are in MHz, with one standard deviation in parentheses. The last column, labeled "Global fit," contains the results of a fit by Farley, MacAdam, and Wing [9] to a large number of intervals in different n and L. The spin-averaged interval $10\bar{D}-10\bar{F}$ is a weighted average of the four intervals, which removes nearly all of the spin dependence, and is defined in Eq. (14).

Interval	This work	Direct measurement	Global fit
$10\,^1D_2-{}^+F_3$	10 918.826(37)	10 918.890(50)	10 918.797(53)
$10\,^3D_1-{}^3F_2$	15 760.667(17)	15 760.670(141)	15 760.707(81)
$10\,^3D_3-{}^3F_4$	15 781.991(11)	15 782.014(50)	15 782.101(74)
$10\,^3D_2-{}^-F_4$	15 770.704(15)	15 770.824(113)	15 770.554(67)
$10\bar{D}-10\bar{F}$	14 560.650(13)	14 560.706(41)	14 560.651(34)

TABLE VIII. Energies of 10D states relative to the He(1s, $n=10$) binding energy (all energies are in MHz, with one standard deviation in parentheses). The 10K energies are calculated by Drake [21] and are expected to be accurate to better than 1 kHz. The 10D-10K intervals are obtained by adding the intervals measured in this work to those measured by Hessels *et al.* [13,14]. The implied energy of each 10D state relative to the hydrogenic level for $n=10$ helium is the sum of these two energies. The energies in the last column of the table represent experimental reference levels in helium; the position of each 10D state is experimentally known to better than 40 kHz.

State	Calculated K energy (MHz)	D-K interval from experiment (MHz)	Implied energy (MHz)
$10\,^1D_2$	$E(^+K_7)$: −54.859 90	−13 636.976(37)	−13 691.836(37)
$10\,^3D_1$	$E(^3K_6)$: −57.519 72	−18 503.129(19)	−18 560.649(19)
$10\,^3D_2$	$E(^-K_7)$: −64.238 87	−18 531.775(17)	−18 596.014(17)
$10\,^3D_3$	$E(^3K_8)$: −60.731 88	−18 537.750(13)	−18 598.482(13)

The four intervals listed in the "final result" row of Table VI can be combined to form the spin-averaged interval, which is often used in comparisons with theory. As discussed by Hessels *et al.*, [14] the spin-averaged (or mean) energy of a manifold of four helium 10L levels is given by a statistically weighted average of the four energies as follows:

$$E(L_{\rm mean})=\frac{1}{8L+4}[(2L+1)E(^+L_L)+(2L+1)E(^-L_L)+(2L-1)E(^3L_{L-1})+(2L+3)E(^3L_{L+1})]\ . \quad (13)$$

The difference between the mean energies of the levels 10L and 10($L+1$) is then obtained by subtracting the above mean energies for the two L values. This difference turns out to be a spin-weighted average of the four measured intervals plus a small correction that is dependent on the magnetic fine structure of the higher-L manifold:

$$\nu_{\bar F}-\nu_{\bar D}=\tfrac{1}{4}[\nu(^+F_3-{}^1D_2)+\nu(^-F_3-{}^1D_2)+\tfrac{3}{5}\nu(^3F_2-{}^3D_1)+\tfrac{7}{5}\nu(^3F_4-{}^3D_3)]+\tfrac{1}{35}\nu(^3F_2-{}^3F_4)\ . \quad (14)$$

The last term must be obtained from either predictions or experimental measurements of the magnetic fine structure of the 10F states. However, the coefficient in front of this energy difference is approximately equal to 0.029 for the 10D-10F mean interval; thus the magnetic fine-structure energy difference must be known only to about 35 kHz in order that the correction term not add more than a 1 kHz uncertainty to the calculation of the mean interval. We use the 10F magnetic fine-structure interval derived by combining direct measurements of the 10G triplet fine-structure interval [28] with measurements of the two triplet 10F-10G intervals [13] to yield $10\,^3F_2-10\,^3F_4=16.484(25)$ MHz. It is evident that the experimental uncertainty in this value contributes a negligible amount to the uncertainty in the mean 10D-10F interval. The experimental mean 10D-10F interval derived from the present measurements is then 14 560.650(13) MHz. The experimental uncertainty in the determination of the mean 10D-10F interval is determined by combining the (uncorrelated) statistical uncertainties in the frequencies of the four measured intervals and then combining this uncertainty in quadrature with the uncertainty in the systematic corrections. The fractional uncertainty in the mean interval is about one part in 10^6. This is very slightly smaller than the fractional uncertainties in the measurements of the higher-L intervals. The absolute uncertainty in the 10D-10F interval, however, is much larger than the absolute uncertainties in the higher-L intervals.

V. DISCUSSION OF RESULTS

The results of the present experiment are compared with the less precise results of Farley, MacAdam, and Wing [9] in Table VII. There are two comparisons in the table because of the way Farley, MacAdam, and Wing [9] reported their results. They presented direct measure-

TABLE IX. Comparison of experimental intervals with theory of Drake [21], including the small retardation contribution $\Delta V''_{\rm ref}$ (in MHz). The individual intervals are in good agreement with theory, as is the spin-averaged interval 10$\bar D$-10$\bar F$ [defined in Eq. (14)].

Interval	This work	Theory	Present measurement minus theory
$10\,^1D_2-{}^+F_3$	10 918.826(37)	10 918.8190(15)	+0.007(37)
$10\,^3D_1-{}^3F_2$	15 760.667(17)	15 760.6848(13)	−0.018(17)
$10\,^3D_3-{}^3F_4$	15 781.991(11)	15 782.0134(13)	−0.022(11)
$10\,^3D_2-{}^-F_4$	15 770.704(15)	15 770.6826(13)	+0.021(15)
10$\bar D$-10$\bar F$	14 560.650(13)	14 560.6523(18)	−0.002(13)

ments of the intervals and they also presented the results of fitting a model of the fine structure to not only their measurements of the $10D$-$10F$ intervals, but also to their measurements of intervals for other values of n and L. The agreement between the current measurements and the previous direct measurement results is good, but a comparison with the global fit results shows only fair agreement.

The results of these experiments allow us to obtain almost purely experimental determinations of the absolute energies of the four $10D$ states. These absolute energies could be of considerable use in laser spectroscopy. (For example, a measurement of the $2\,^1S-10\,^1D$ interval, similar to the measurements of Lichten, Shiner, and Zhou [29], could be used to deduce the absolute energy of the $2\,^1S$ state with very little reliance on theory.) These determinations are accomplished as follows. The intervals measured in this work are combined with the intervals previously measured by Hessels *et al.* [13,14] to obtain the total energy differences between the four $10D$ states and the four corresponding $10K$ states. The experimental $10D$-$10K$ intervals are shown in Table VIII. These energy differences are then combined with calculations of the binding energy of the $10K$ states relative to the He($1s$, $n=10$) level. The $10K$ energies have been calculated in two very different formalisms by Drachman [19] and by Drake [21] and the two calculations are in excellent agreement. Combining the theoretical predictions with the $10D$-$10K$ intervals yields absolute energies for the $10D$ levels, as shown in Table VIII. These could be very useful as reference levels for the spectroscopic determination of absolute binding energies of lower-L states.

We compare the intervals obtained in this work with theory in Table IX. This theory includes the high-precision variational calculations of Drake [21], the relativistic and the QED contributions included by Drake [21], and also a small contribution $\Delta V''_{\rm ret}$ discussed in Ref. [1]. A comparison of the results of this work with the calculated values shown in Table IX shows good agreement both for the individual measurements and for the mean interval. The fact that each of the four individual intervals agree with theory indicates that the spin-structure calculations of Drake [21] for the D and the F states are accurate at the level of our experimental precision. The agreement of the mean interval with theory is in stark contrast to the situation at high L, where systematic discrepancies exist. This pattern of discrepancies is shown in Table X and is also illustrated in Fig. 8, where it can be seen that the higher-L intervals are systematically about 6 ppm smaller than (and clearly inconsistent with) the theoretical predictions, whereas the $10D$-$10F$ interval agrees with theory. Where discrepancies exist, they are much smaller than the total contribution of retardation to the interval (represented by $\Delta V_{\rm ret}$ in Table X) but comparable to or larger than $\Delta V''_{\rm ret}$, the portion of $\Delta V_{\rm ret}$ thought not to be implicitly included in Drake's calculation.

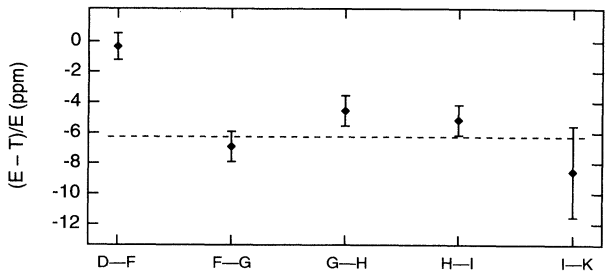

FIG. 8. Graphic comparison of the discrepancies with theory of the various intervals measured in $n=10$ helium. The $10D$-$10F$ interval agrees precisely with theory, while the higher-L intervals are all smaller than the theoretical predictions by about 6 ppm, clearly inconsistent with the theoretical predictions. The discrepancies at higher L may indicate the presence of alternative physics, beyond the standard approximation of atomic theory, for large-sized atoms. The discrepancies are so far not explained.

The fact that the discrepancies are confined to high-L states in which the Rydberg electron is always at large distances from the core suggests that there is yet interesting new physics to be understood for large-sized atoms. In fact, the suggestion that such physics (specifically the Casimir or retardation interactions) might be present in these large-sized atoms was the initial motivation for this series [12–14] of helium Rydberg measurements. Detailed calculations [17,18,30,31] of the dipole retardation contributions have been carried out by a number of techniques and it is clear that for the high-L, large-sized states, methods that go beyond the standard approximation of atomic theory are required. This fact is illustrated, for instance, by the contributions of $\Delta V''_{\rm ret}$ shown in Table X, which cannot be obtained from standard atomic theory calculations. The fact that the high-L states still show systematic discrepancies may indicate either that the retardation corrections have not yet been calculated with the required precision or that other relativistic effects are also modified at large distances.

TABLE X. Comparison of the discrepancies between theory and measurements of $n=10$ mean fine-structure intervals in helium (all values in kHz). Theory (T) is from Table I and includes the contribution of $\Delta V''_{\rm ret}$ (shown separately in the last column). Experiment (E) is also from Table I, except for the D-F interval, where the present result is used. The column labeled $\Delta V_{\rm ret}$ shows the full contribution of retardation to each measured interval and is taken from Ref. [18]. The column labeled $\Delta V''_{\rm ret}$ is the portion of the retardation contribution thought not be implicitly included in Drake's calculations (taken from Ref. [31]).

Interval	$E-T$	$\Delta V_{\rm ret}$	$\Delta V''_{\rm ret}$
$10I$-K	−0.52(20)	−4.52	−0.30
$10H$-I	−0.82(23)	−12.64	−0.45
$10G$-H	−2.28(49)	−42.20	−0.71
$10F$-G	−14.3(22)	−185.33	−1.22
$10D$-F	−2(13)	−1329.9	−2.40

ACKNOWLEDGMENTS

This work was supported by the National Science Foundation under Grants Nos. PHY90-19064 and PHY93-96235. We would also like to acknowledge the assistance of Dr. Francis Deck.

[1] Stephen R. Lundeen, in *Long-Range Casimir Forces: Theory and Recent Experiments on Atomic Systems,* edited by Frank S. Levin and David A. Micha (Plenum, New York, 1993), pp. 73–105.
[2] H. J. Beyer and K. J. Kollath, J. Phys. B **11**, 979 (1978).
[3] W. H. Wing, D. L. Mader, and W. E. Lamb, Jr., Bull. Am. Phys. Soc. **16**, 531 (1971).
[4] W. E. Lamb, Jr., D. L. Mader, and W. H. Wing, in *Fundamental and Applied Laser Physics: Proceedings of the Esfahan Symposium,* edited by M. S. Feld, A. Javan, and N. Kurnit (Wiley, New York, 1973), pp. 523–548.
[5] W. H. Wing, K. R. Lea, and W. E. Lamb, Jr., in *Atomic Physics 3,* edited by S. J. Smith and G. K. Walters (Plenum, New York, 1973), pp. 119–141.
[6] Keith B. MacAdam and William H. Wing, Phys. Rev. A **12**, 1464 (1975).
[7] Keith B. MacAdam and William H. Wing, Phys. Rev. A **13**, 2163 (1976).
[8] Keith B. MacAdam and William H. Wing, Phys. Rev. A **15**, 678 (1977).
[9] John W. Farley, Keith B. MacAdam, and William H. Wing, Phys. Rev. A **20**, 1754 (1979); **25**, 1790(E) (1982).
[10] William H. Wing and Keith B. MacAdam, in *Progress in Atomic Spectroscopy,* edited by W. Hanle and H. Kleinpoppen (Plenum, New York, 1978), pp. 491–527.
[11] D. R. Cok and S. R. Lundeen, Phys. Rev. A **23**, 2488 (1981).
[12] S. L. Palfrey and S. R. Lundeen, Phys. Rev. Lett. **53**, 1141 (1984).
[13] E. A. Hessels, F. J. Deck, P. W. Arcuni, and S. R. Lundeen, Phys. Rev. A **41**, 3663 (1990); **44**, 7855(E) (1991).
[14] E. A. Hessels, P. W. Arcuni, F. J. Deck, and S. R. Lundeen, Phys. Rev. A **46**, 2622 (1992).
[15] Y. Kriescher, O. Hilt, and G. v. Oppen, Z. Phys. D **29**, 103 (1994).
[16] Edward J. Kelsey and Larry Spruch, Phys. Rev. A **18**, 15 (1978); **18**, 845 (1978); **18**, 1055 (1978).
[17] C. K. Au, G. Feinberg, and J. Sucher, Phys. Rev. Lett. **53**, 1145 (1984).
[18] James F. Babb and Larry Spruch, Phys. Rev. A **38**, 13 (1988).
[19] R. J. Drachman, Phys. Rev. A **31**, 1253 (1985); **38**, 1659(E) (1988); in *Long-Range Casimir Forces: Theory and Recent Experiments on Atomic Systems* (Ref. [1]), pp. 219–272.
[20] E. A. Hessels, Phys. Rev. A **46**, 5389 (1992).
[21] G. W. F. Drake and Zong-Chao Yan, Phys. Rev. A **46**, 2378 (1992); Gordon W. F. Drake, in *Long-Range Casimir Forces: Theory and Recent Experiments on Atomic Systems* (Ref. [1]), pp. 107–217.
[22] W. G. Sturrus, E. A. Hessels, P. W. Arcuni, and S. R. Lundeen, Phys. Rev. A **44**, 3032 (1991).
[23] Nelson E. Claytor, Ph.D. thesis, University of Notre Dame, 1994 (unpublished).
[24] G. W. F. Drake, Adv. At. Mol. Opt. Phys. **32**, 93 (1993).
[25] S. R. Lundeen, Ph.D. thesis, Harvard University, 1975 (unpublished).
[26] K. A. Safinya, Ph.D. thesis, Harvard University, 1979 (unpublished).
[27] John W. Farley and William H. Wing, Phys. Rev. A **23**, 2397 (1981).
[28] E. A. Hessels, W. G. Sturrus, S. R. Lundeed, and David A. Cok, Phys. Rev. A **35**, 4489 (1987).
[29] W. Lichten, D. Shiner, and Zhi-Xiang Zhou, Phys. Rev. A **43**, 1663 (1991).
[30] Larry Spruch, Phys. Today **39** (11), 37 (1986).
[31] C. K. Au and M. A. Mesa, Phys. Rev. A **41**, 2848 (1990).